Volume xx (200y), Number z, pp. 1–13

Solid Geometry Processing on Deconstructed Domains

Silvia Sellán[1] Herng Yi Cheng[2] Yuming Ma[3] Mitchell Dembowski[4] Alec Jacobson[3]

[1]University of Oviedo [2]Massachusetts Institute of Technology [3]University of Toronto [4]Ryerson University

arXiv:1807.00866v1 [cs.GR] 2 Jul 2018

Abstract

Many tasks in geometry processing are modeled as variational problems solved numerically using the finite element method. For solid shapes, this requires a volumetric discretization, such as a boundary conforming tetrahedral mesh. Unfortunately, tetrahedral meshing remains an open challenge and existing methods either struggle to conform to complex boundary surfaces or require manual intervention to prevent failure. Rather than create a single volumetric mesh for the entire shape, we advocate for solid geometry processing on deconstructed domains*, where a large and complex shape is composed of overlapping solid subdomains. As each smaller and simpler part is now easier to tetrahedralize, the question becomes how to account for overlaps during problem modeling and how to couple solutions on each subdomain together* algebraically*. We explore how and why previous coupling methods fail, and propose a method that couples solid domains only along their boundary surfaces. We demonstrate the superiority of this method through empirical convergence tests and qualitative applications to solid geometry processing on a variety of popular second-order and fourth-order partial differential equations.*

1. Introduction

Many tasks in computer graphics and geometry processing can be modeled mathematically as solutions to partial differential equations (PDEs) over a compact spatial domain. For example, shape-aware scattered data interpolation can be modeled as a solution to the Laplace equation ($\Delta u = 0$). Smooth detail-preserving shape deformations can be efficiently parametrized using solutions to a bi-Laplace equation ($\Delta^2 u = 0$). Even computation of geodesic distances can be captured via iterative solutions to a Poisson equation ($\Delta u = f$). These applications — and many others — rely on *discretization* to realize their solutions on the complex shapes found throughout computer graphics. The most common discretization is via the finite-element method (FEM) using piecewise-linear functions defined over a simplicial mesh. For problems over solid regions in $\mathbb{R}^3$, this typically requires constructing a tetrahedral mesh that fills the volume bounded by a given surface. Compared to regular grids, unstructured tetrahedral meshes afford spatially varying resolution and complex boundary surfaces — *in theory, at least*.

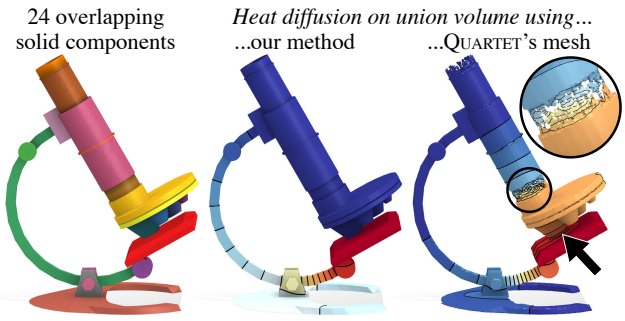

Figure 1: TETGEN *fails to tetrahedralize this Microscope, even after preprocessing the input using [ZGZJ16].* QUARTET *successfully outputs a tet mesh, but thin parts are poorly approximated (inset) and close features are merged (arrow).*

In practice, constructing tetrahedral meshes is a fragile process. While the application of linear FEM is often straightforward after posing a problem in the smooth setting, the actual creation of a valid tetrahedral mesh inside a triangle mesh is often left to an *ad hoc* patchwork of heuristics including manual intervention and mesh repair. Existing automatic meshing methods fall short. They either fail too often, create too poor quality elements, or approximate too loosely the input domain boundary, as shown in Figure 1.

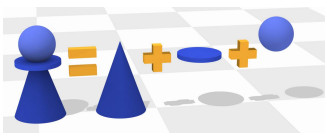

We consider an interesting class of shapes that are — at least conceptually if not literally — described as the union of simpler domains (see inset). The traditional conforming tetrahedralization pipeline would proceed by first computing the result of a surface mesh union operation and then attempt to mesh the interior. However, even if the input triangle meshes are "clean", the exact mesh boolean result may be host to a number of issues that trip up available tetrahedralization heuristics: fine features, small voids, and poorly shaped elements (see Figure 2). In general, the *exact* result introduces many new vertices whose coordinates are rational numbers. Naively rounding such vertices to floating-point coordinates may introduce self-intersections, and efficient rounding while preventing intersections in 3D is still an open problem [For97].

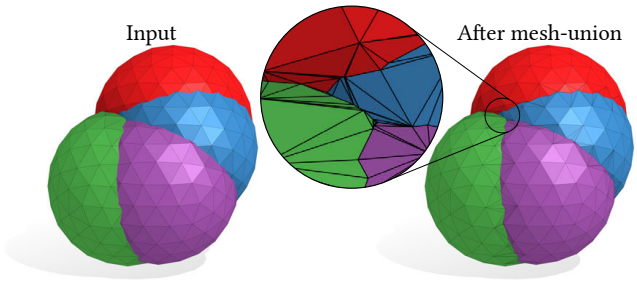

Figure 2: *Even if all input meshes are "clean" (e.g., four overlapping geodesic spheres on left), their exact mesh-union may have arbitrarily poor quality triangles. These in turn trip up conforming Delaunay tet-meshers: e.g., TetGen [Si03] fails on this example.*

In this paper, we propose an alternative to this error-prone pipeline. We consider inputs as *deconstructed domains*, composed as the union of any number of simpler shapes. We tetrahedralize subdomains independently with no requirement to share vertex positions or combinatorics. Subdomains are treated democratically, without a priority ordering or hierarchy. We then couple discrete PDEs or variational problems defined on each domain *algebraically*.

This coupling requires care. The given PDE or variational problem must be adapted for overlapping domains to avoid bias or double-counting in twice-covered regions. Via null-space analysis, we show that naive equality constraints leads to *locking*, artificial error that does not vanish under resolution refinement.

We borrow ideas from domain decomposition and immersed boundary methods to derive a general-purpose boundary-only coupling in the smooth setting and then demonstrate its effectiveness for linear FEM discretizations of common problems in 1D, 2D, and 3D (e.g., Poisson equations). Domains are coupled with hard constraints resulting in a parameterless method. Further, we extend our results to boundary-only higher-order coupling for applications of mixed FEM for fourth-order problems (e.g., bi-Laplace equation).

2. Related Work

Our goal is to improve the robustness of geometry processing that requires solving partial differential equations (PDEs) on solid shapes.

PDE Solvers in Geometry Processing Improving the accuracy, robustness and performance of solvers for geometry problems is a core area of interest [BBK05, KFS13, Kaz15, DMZ*17, HDA17, SPSH*17]. While we focus on robustness with respect to the input representation, our work relates to these as an *algebraic* preprocess or filter on the eventual linear system or optimization problem. This is in contrast to geometric approaches to robustness such as remeshing [BK04b, SRUL16, GJTP17] or enclosing a shape in a cage [JMD*07, SVJ15]. For example, using the boundary element method avoids volumetric meshing altogether (e.g., [JP99, DHB*16, SVB17]), however, this also limits the class of problems that can be solved. In contrast to methods specific to one application (e.g., character skinning [BTST12]), our method applies to a general class of PDEs.

Constructive Solid Geometry Emerging technologies such as 3D printing and virtual reality have ignited broader interest in geometric modeling. The result is that we have a huge amount of geometric data, but that data is rarely composed of a single, watertight, non-self-intersecting, oriented manifold surface [ZJ16]. Instead, people create using constructive solid geometry tools like OpenSCAD and TinkerCAD that happily allow overlapping simpler models to create a larger, more complex shape. Early digital constructive solid geometry complements this modeling paradigm with fast evaluation using implicit functions (e.g., [WMW86]) and GPU-friendly rendering [GHF86]. While the complexity of available meshed surface geometry grows, researchers have devised interesting and interactive ways to create complex models using preexisting detailed parts [GSP*06, CK10, CKGK11].

Most volumetric solvers do not consider the upstream modeling process and instead require a single volumetric mesh as input. This puts a heavy burden on modeling tools to maintain a clean surface geometry via mesh "surgery" operations [SBSCO06, SS10a, SS10b]. Despite recent progress on robust boolean operations for triangle meshes [BF09, BGF15, ZGZJ16], the resulting meshes may have arbitrarily poor aspect ratio (see Figure 2) preventing or damaging tetrahedralization. In contrast, we operate directly on the overlapping subdomain representation common to solid modeling.

Tetrahedral Meshing Although our work is an effort to subvert tetrahedral meshing and its issues, we still rely heavily on the progress and open source software from this literature. The fundamental challenge at the core of tetrahedral meshing is the balance between ensuring high-quality elements (see, e.g., [She02]) and conforming to a given input surface. While a complete meshing survey is outside the scope of this paper, we identify issues and previous works as they relate to our setting.

Conforming Delaunay Tetrahedralization methods maintain the input geometry (and combinatorics) exactly by inserting input vertices and faces into a Delaunay triangulation and then improving element quality via local operations and additional Steiner vertices [CDS12]. In practice, the software TetGen [Si03] implements many state-of-the-art algorithms and heuristics. The success rate of TetGen is not 100% (see Figure 3), but it succeeds far more often

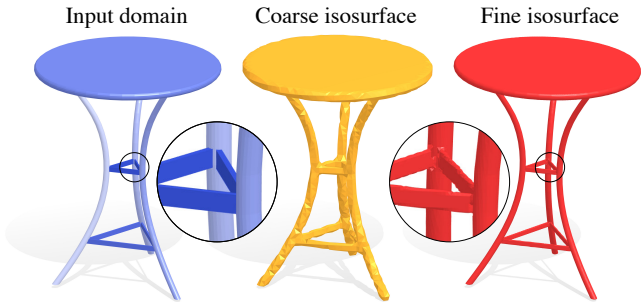

Figure 3: *This seemingly innocuous union (left) causes the conforming Delaunay method* TetGen *[Si03] to fail. Implicit or query-based methods have trouble capturing fine structures (middle) without resorting to high resolutions (right).*

when inputs are smaller and simpler, without spatially close parts or small triangles. We use TETGEN in most of our examples, but run it on each subdomain, rather than the complex, complete shape.

Alternatively, other meshing methods work by employing a background grid [LS07] or implicit representation of the input shape [ACSYD05]. These methods ensure good quality elements by construction, but struggle to closely approximate the input shape geometry — especially in the presence of sharp features. Doran et al. [DCB13] provide an open source implementation, QUARTET and while robust in the sense of successfully outputting a mesh, this method will join together close features and fail to resolve thin parts (see Figure 1). In contrast to Cuilliere et al. [CFD12], we avoid computing a unified mesh and do not require matching or correspondence between vertices or combinatorics of overlapping meshes.

Domain Decomposition The idea of coupling solutions to partial differential equations across overlapping domains is quite old [Sch70] and well studied. The majority of previous methods for overset and non-matching grids focus on domain decomposition for parallel, offline computation using iterative solvers [SBGG04]. Alternatively, *immersed boundary methods* [Pes73] use similar constraints to couple the simulation of one or many objects embedded in a background simulation. For example, coupling a floating elastic body to a fluid simulation (e.g., [GSLF05]).

In contrast, our interest is in reducing the burden of tetrahedralization while maintaining the complexity of shapes found in graphics and geometry processing. We treat coupling as a hard constraint to single linear system solved using modern, large sparse linear solvers (e.g., [Dav06, AA00]). No sub-domain has preference over another.

English et al. [EQYF13] simulate water at varying resolutions by allowing regular finite-difference grids to rigidly overlap. Their method assigns priorities to grids and stitches higher-priority grids along their boundaries into lower-priority grids to solve a Poisson equation. Similar so-called *Chimera grids* [Ben85] are found in early fluid simulations on comparatively simple domains [BSD83, Hen94, KKRC97, DMYN08]. Henshaw describes how boundary values of one grid are interpolated using ghost points. This method is applied to overlapping regular Cartesian or polar grids. Malgat et al. [MGL*15] couple overlapping discretizations for elasticity simulation via energy minimization. Their method requires a hierarchical ordering.

Overset grid methods (e.g., [Nak99, LSLR01, BS15]) often assume that the domain has been designed with an overlapping solver in mind. High resolution grids near important areas naturally have well defined and known priority over coarse background grids. Instead, we consider the case where subdomain priorities are not known and domains merely serve as an overlapping subdivision. The resolution of a single grid may itself be adaptive.

Schwarz domain decomposition can be interpreted in the context of discontinuous Galerkin finite element method (DGFEM) or extended FEM (XFEM) [Kau12], where subdomains are interpreted as large, high-degree elements and coupling is analogous to interface conditions. Edwards & Bridson [EB15] propose such a solver for Poisson, elasticity and bi-Laplace problems. Their overlapping subdomains are extracted from a unified grid of the entire domain.

3. Smooth Foundations

We first consider a partial differential equation (PDE) involving a smooth function u defined over a volumetric (i.e., co-dimension zero) domain $\Omega \subset \mathbb{R}^d$ with appropriate boundary conditions applied to u on the boundary of the domain $\partial\Omega$. We focus specifically on elliptic PDEs resulting from energy minimizations common in geometry processing. For example, minimizing the squared gradient (i.e., Dirichlet energy) minus a unit potential, subject to fixing the value of u to a known function g on the boundary of the domain,

$$\min_u \int_\Omega \left(\tfrac{1}{2}\|\nabla u\|^2 - u\right) dA \tag{1}$$

$$\text{subject to } u(\mathbf{x}) = g(\mathbf{x}) \qquad \forall \mathbf{x} \in \partial\Omega, \tag{2}$$

results in the second-order Poisson equation on the interior,

$$\Delta u = 1 \qquad \forall \mathbf{x} \in \Omega. \tag{3}$$

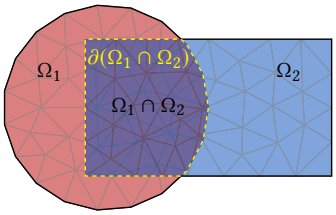

Suppose we are incapable of measuring an energy directly over all of the domain Ω, but instead are only able to measure energies over two *overlapping* subdomains $\Omega_1, \Omega_2 \subset \mathbb{R}^d$ whose union composes the original domain $\Omega_1 \cup \Omega_2 = \Omega$. By replacing u with new u_1 and u_2 over each respective subdomain, we can write the original minimization problem in Equation (1), breaking the integral into the non-overlapping parts in each subdomain ($\Omega_1 \setminus \Omega_2$ and $\Omega_2 \setminus \Omega_1$) and their intersection ($\Omega_1 \cap \Omega_2$) and adding a *pointwise* equality coupling constraint,

$$\min_{u_1,u_2} \int_{\Omega_1 \setminus \Omega_2} \left(\tfrac{1}{2}\|\nabla u_1\|^2 - u_1\right) dA + \tag{4}$$

$$+ \int_{\Omega_2 \setminus \Omega_1} \left(\tfrac{1}{2}\|\nabla u_2\|^2 - u_2\right) dA + \tag{5}$$

$$+ \frac{1}{2}\int_{\Omega_1 \cap \Omega_2} \left(\tfrac{1}{2}\|\nabla u_1\|^2 - u_1 + \tfrac{1}{2}\|\nabla u_2\|^2 - u_2\right) dA \tag{6}$$

$$\text{subject to } u_1(\mathbf{x}) = g(\mathbf{x}) \qquad \forall \mathbf{x} \in \partial\Omega \cap \partial\Omega_1, \tag{7}$$

$$\text{and } u_2(\mathbf{x}) = g(\mathbf{x}) \qquad \forall \mathbf{x} \in \partial\Omega \cap \partial\Omega_2, \tag{8}$$

$$\text{and } u_1(\mathbf{x}) = u_2(\mathbf{x}) \qquad \forall \mathbf{x} \in \Omega_1 \cap \Omega_2. \tag{9}$$

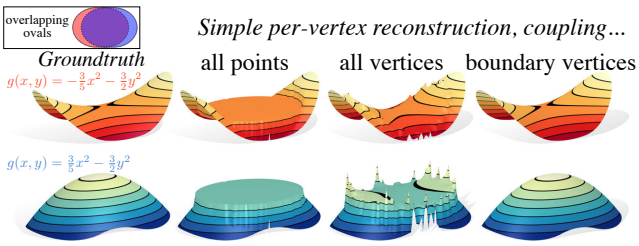

Figure 4: *The constraint space is unrelated to the energy. Consider a simple reconstruction energy* $\min_u \int_{\Omega_1 \cup \Omega_2} (u-g)^2\, dA$. *Constraining* all points *in the overlap locks to a linear function;* all vertices *looks promising for saddle-shaped functions, but cannot reproduce positive curvature functions;* boundary vertices *avoids locking.*

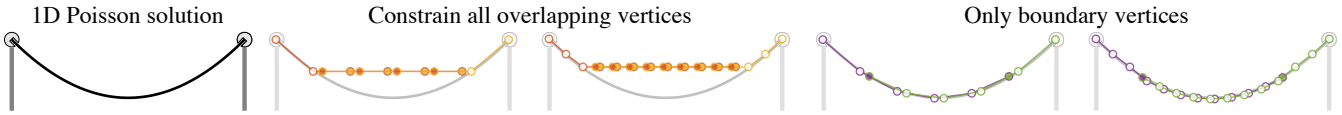

Figure 5: *Left-to-right: the Poisson solution in 1D is a simple parabola, easily approximated using linear finite element method. If the discrete domain is given as two overlapping meshes (red & yellow), then enforcing equality at* all vertices *in the overlap results in the solution* locking *to a linear function. This problem does not go away with mesh refinement. Coupling the meshes only at the sub-domain boundary (purple & green) alleviates locking, and converges with refinement.*

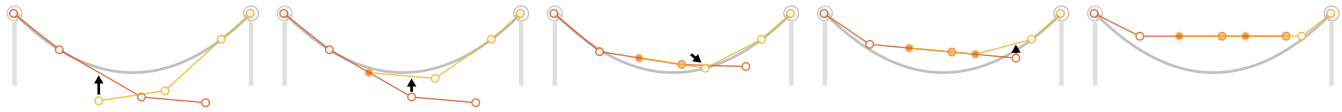

Figure 6: *Locking occurs at any scale and can be understand as a "Domino effect" when enforcing constraints one-by-one. In 1D, consecutive constraints force the solution to a line: eventually the entire overlapping region must be a single line.*

Advantage of working with energies The appearance of the $\frac{1}{2}$ factor before the integrated energy in the intersection $\Omega_1 \cap \Omega_2$ region (see Equation (6)) would not be so obvious if we had worked with the Poisson problem directly as a PDE (see Equation (3)). However, viewed as variational problem, the necessity of the $\frac{1}{2}$ is clear: we should not double count the energy contributed in this region.

4. Discrete Locking

The deconstructed energy optimization problem in Equation (4) only involves first derivatives and linear equality constraints. It is tempting to jump to a finite element method (FEM) discretization using piecewise-linear elements for each subdomain Ω_1 and Ω_2, e.g., hat functions (over polylines for $d = 1$, triangle meshes for $d = 2$ and tetrahedral meshes in $d = 3$)

$$u_i(\mathbf{x}) = \sum_{j=1}^{n} u_{ij}\varphi_{ij}(\mathbf{x}), \tag{10}$$

with interpolated values at the n vertices given as a vector $\mathbf{u}_i \in \mathbb{R}^n$.

If the meshes over Ω_1 and Ω_2 have *only and exactly* coincident vertices *and* compatible combinatorics in the intersection region $\Omega_1 \cap \Omega_2$, then we call them *matching*. In this special case, enforcing the point-wise equality constraint in Equation (9) is equivalent to merging the meshes. The solution search space is exactly as rich as linear FEM over the merged mesh.

For meshes with vertices in general position, perfect coincidence never happens. Pointwise equality immediately reduces the search space to piecewise linear functions that exist mutually in both linear FEM function spaces over the intersection $\Omega_1 \cap \Omega_2$. In the general *non-matching* case, the constraint reduces the search space dramatically: *only* functions that take on a linear function over $\Omega_1 \cap \Omega_2$ remain (see Figure 4, left).

This is an extreme case of what is known as *locking* in the FEM literature [ZT00]. Locking is an artificial stiffening of system during discretization. In our case, the constraints are so strict that only rather boring functions remain. These functions can be arbitrarily far from the desired solution and discretization refinement by adding more (general position) vertices will not help (see Figure 5).

4.1. Constraints at All Vertices Causes Locking

One immediate strategy is to require equality only at mesh vertices. This ties the values at one mesh's vertices to the piecewise linearly interpolated value on the other mesh via a linear equality constraint and *vice-versa*, e.g.,:

$$u_{1i} = \sum_{j=1}^{n_2} u_{2j}\varphi_{2j}(\mathbf{v}_{1i}) \qquad \forall i \text{ such that } \mathbf{v}_{1i} \in \Omega_1 \cap \Omega_2, \tag{11}$$

$$u_{2j} = \sum_{i=1}^{n_1} u_{1i}\varphi_{1i}(\mathbf{v}_{2j}) \qquad \forall j \text{ such that } \mathbf{v}_{2j} \in \Omega_2 \cap \Omega_1, \tag{12}$$

where $\mathbf{v}_{ki} \in \mathbb{R}^d$ is the position of the ith vertex in the mesh over subdomain Ω_k. The coefficients obtained by evaluating the hat functions $\varphi_{\ell j}(\mathbf{v}_{ki})$ of the *other* mesh over subdomain Ω_ℓ are simply the barycentric coordinates of $\mathbf{v}_{ki}$ in the containing simplex (e.g., tetrahedron for $d = 3$).

We can collect these constraints in matrix form

$$\mathbf{C}\begin{pmatrix} \mathbf{u}_1 \\ \mathbf{u}_2 \end{pmatrix} = \mathbf{0}, \tag{13}$$

where $\mathbf{C} \in \mathbb{R}^{(m_1+m_2)\times(n_1+n_2)}$ is a sparse rectangular matrix, where each row corresponds to one of the m_1 vertices of the mesh over Ω_1 lying in Ω_2 or *vice-versa*.

These linear equality constraints are easy to implement in practice (e.g., via the null space or Lagrange multiplier method). Unfortunately, these constraints do not alleviate locking.

In $\mathbb{R}^1$, constraining all vertices in the overlapping region $\Omega_1 \cap \Omega_2$ is catastrophic. Intuitively, if a segment of the mesh over Ω_1 overlaps with a segment of the mesh over Ω_2 then both pairs of vertices will have to lie on the same line. In the worst case, an alternating order of vertices from Ω_1 and Ω_2 creates a *domino effect*, and the entire intersection region locks to the same linear function (see Figure 6).

It is tempting to extrapolate that these constraints will always result in point-wise locking, but in higher dimensions ($d > 1$), locking from vertex constraints is more nuanced. We observe in Figure 4 that the constraint space created by coupling all vertices struggles to reproduce a round parabolic function and more easily reproduces a saddle-shaped hyperbolic function. Indeed, imposing this constraint when solving a Laplace equation (saddle-shaped solution) we see

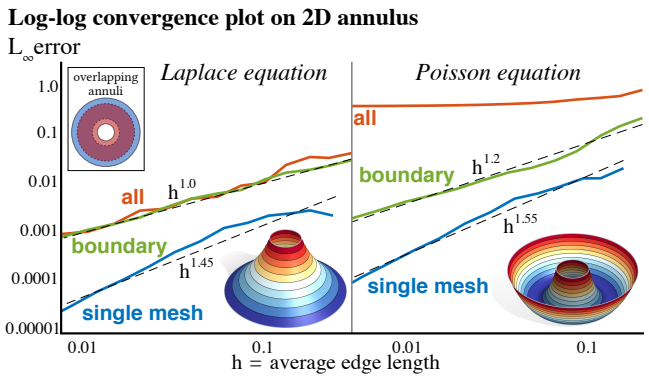

Figure 7: *Constraining* all *vertices in the overlap between two concentric annuli matches the convergence rate of our* boundary only *constraints for* $\Delta z = 0$ *(left). However, constraining* all *does not converge for* $\Delta z = 1$ *(right), while* boundary only *maintains convergence. For reference: a non-overlapping,* single mesh *converges.*

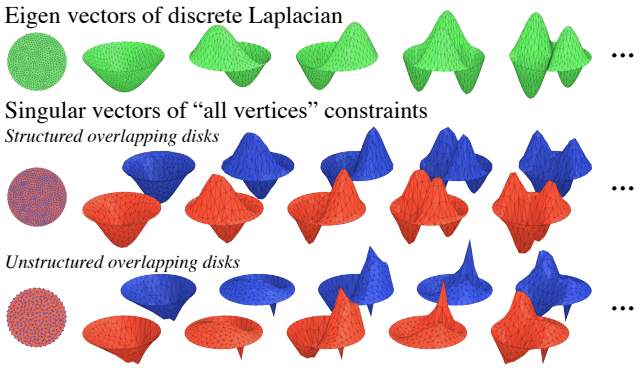

Figure 8: *Eigen modes of the constraint matrix built from fixing all vertices of two overlapping, non-matching disk meshes resemble those of the discrete Laplacian. More irregular meshing produces less smooth modes.*

significantly better convergence with respect to mesh resolution than when solving a parabolic Poisson equation (see Figure 7).

This is not a coincidence. The constraint matrix $\mathbf{C}$ in Equation (13) satisfies many desired properties (constant precision, linear precision, the maximum principle and local support; see [WMKG07]) of a *discrete Laplacian* on the "joint mesh" over $\Omega_1 \cap \Omega_2$ created by connecting each vertex of Ω_1 to the vertices of its containing simplex containing in Ω_2 and *vice-versa*. Performing eigen analysis on $\mathbf{C}$ reveals that it responds as a discrete operator strikingly similarly to the FEM discrete (cotangent) Laplacian (see Figure 8). Due to this relationship, we call the artificial stiffening due to constraining all overlapping vertices *harmonic locking*.

We will defer our discussion of attempting to soften this equality constraint to Section 7 and instead return to the smooth setting to derive a locking-free solution from first principles.

5. Boundary-Only Coupling

The root of the locking troubles is the point-wise equality constraint over the overlapping region $\Omega_1 \cap \Omega_2$ in Equation (9). Surely coupling is crucial. If we remove this constraint entirely, then u_1 and u_2 will solve independent Poisson equations, subject to emergent natural boundary conditions (in this case, $\nabla u \cdot \mathbf{n} = 0$) on the overlap boundary $\partial(\Omega_1 \cap \Omega_2)$. In other words, these zero normal derivative boundary conditions uniquely determine u_1 and u_2.

The fact that minimizers of our energy in Equation (1) are uniquely determined by boundary conditions can be spun to play in our favor when searching for non-locking coupling constraints. Concretely, we will now show that it is sufficient to restrict the pointwise equality constraints from the entire intersection region $\Omega_1 \cap \Omega_2$ in Equation (9) to *only* its boundary $\partial(\Omega_1 \cap \Omega_2)$:

$$u_1(\mathbf{x}) = u_2(\mathbf{x}) \qquad \forall \mathbf{x} \in \partial(\Omega_1 \cap \Omega_2). \tag{14}$$

We must show that minimizing the deconstructed energy in Equation (4) over u_1 and u_2 with this constraint instead of Equation (9) remains equivalent to the minimization over u in Equation (1).

Assume that u_1 and u_2 are minimizers of Equation (4) satisfying $u_1 = u_2|_{\Omega_1 \cap \Omega_2}$, then by uniqueness of energy minimizers and equivalence with the energy in Equation (1), $u = u_1|_{\Omega_1}$ and $u = u_2|_{\Omega_2}$. We must show that minimizing Equation (4) implies that $u_1 = u_2|_{\Omega_1 \cap \Omega_2}$.

Given minimizers u_1 and u_2 of Equation (4), let us define $u_1 = u_2 := h|_{\partial(\Omega_1 \cap \Omega_2)}$. It does not matter that we do not explicitly know the value of h. It is enough that it is well defined implicitly by solving the problem in Equation (4) subject to Equation (14). Since the minimizers u_1 and u_2 satisfy the Dirichlet conditions on their respective boundaries (Equations (7-8)), we can add the following constraints to Equation (4) without changing the minimum:

$$u_1(\mathbf{x}) = u_2(\mathbf{x}) = h(\mathbf{x}) \qquad \forall \mathbf{x} \in \partial(\Omega_1 \cap \Omega_2). \tag{15}$$

Minimizers to our quadratic energy are uniquely determined by the values on the boundary of the domain, so we can isolate the problem for the overlapping region $\Omega_1 \cap \Omega_2$, for example:

$$\min_{u_1} \tfrac{1}{2} \int_{\Omega_1 \cap \Omega_2} \tfrac{1}{2} \|\nabla u_1\|^2 - u_1 \, dA \tag{16}$$

$$\text{subject to } u_1(\mathbf{x}) = h(\mathbf{x}) \qquad \forall \mathbf{x} \in \partial(\Omega_1 \cap \Omega_2), \tag{17}$$

whose optimal argument is identical to the analogous problem replacing u_1 with u_2, thus implying that the two functions agree on the overlapping region: $u_1 = u_2|_{\Omega_1 \cap \Omega_2}$.

Schwarz noticed this over a century ago [Sch70]. Since then, it has been been exploited for domain decomposition for parallelization and memory decoupling for iterative solvers discussed in Section 2.

Analogous to the enforcement of Dirichlet boundary conditions, in the discrete linear FEM setting, we constrain only boundary vertices of Ω_1 lying inside the other domain Ω_2 or *vice-versa*:

$$u_{1i} = \sum_{j=1}^{n_2} u_{2j} \varphi_{2j}(\mathbf{v}_{1i}) \qquad \forall i \text{ such that } \mathbf{v}_{1i} \in \partial\Omega_1 \cap \Omega_2, \tag{18}$$

$$u_{2j} = \sum_{i=1}^{n_1} u_{1i} \varphi_{1i}(\mathbf{v}_{2j}) \qquad \forall j \text{ such that } \mathbf{v}_{2j} \in \partial\Omega_2 \cap \Omega_1. \tag{19}$$

These constraints are a subset of the rows of $\mathbf{C}$ in Equation (11), and we call this much smaller matrix $\mathbf{A} \in \mathbb{R}^{(b_1+b_2)\times(n_1+n_2)}$, where the mesh of Ω_i has b_i overlap-boundary vertices.

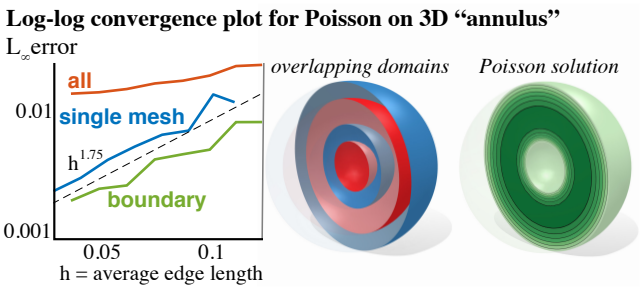

Figure 9: *Constraining* all *vertices between two concentric spherical shells ("3D annuli"; cut view in middle) does not appear to converge for the Poisson equation* $\Delta u = 1$ *(right), while* boundary only *exhibits similar convergence to a non-overlapping* single mesh.

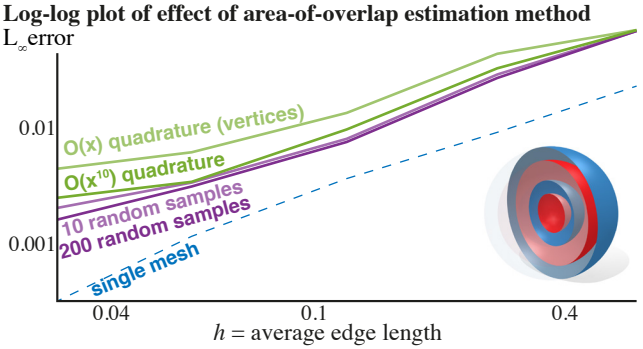

Figure 10: *Quadrature for estimating partial volume at boundary elements can increase convergence, with diminishing returns.*

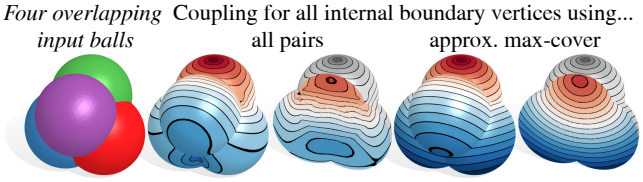

Figure 11: *Boundary coupling across all subdomain pairs leads to messy locking near the overlap boundary (6001 constraints). Instead, our heuristic keeps exactly one constraint per overlap boundary vertex (3893 constraints).*

Not only does fixing the boundary result in a smaller number of constraints and thus typically a better conditioned system, but also the discrete approximations are free of locking artifacts. We see this immediately in the 1D example in Figure 5. The boundary constraints do not show up visible in the constraint space when reproducing hyperbolic or parabolic functions Figure 4. In Figures 7 and 9, convergence with respect to mesh resolution for second-order problems roughly matches that of using a single unified mesh. Recall that we are purposely avoiding creating such a unified mesh, especially in $\mathbb{R}^3$, where mesh surgery and likely manual intervention and parameter tuning would be necessary. Instead, complex shapes can be created by overlapping many solid subdomains and coupling solutions using our proposed boundary-only constraints.

5.1. Multiple Overlapping Subdomains

In general, a complex shape may be composed of the union of $K > 1$ subdomains:

$$\Omega = \bigcup_{i=1}^{K} \Omega_i. \tag{20}$$

All of our derivations so far for $K = 2$ extend easily to $K > 2$. Our deconstructed energy has the form

$$\sum_{i=1} \int_{\Omega} \frac{1}{\sum_{j=1}^{K} \chi_j} \left(\tfrac{1}{2} \|\nabla u_i\|^2 - u_i \right) \, dA, \tag{21}$$

where χ_j is the characteristic function of Ω_j (i.e., $\chi_j(\mathbf{x}) = 1$ for $\mathbf{x} \in \Omega_j$ and $= 0$ otherwise). We defer the implementation details and matrix construction to Appendix A.

Many problems in geometry processing are slight variations on the minimization of this energy. For example, implicit time-integrations of the wave equation replace the unit potential with acceleration, while the heat equation replaces this with a temperature field [SCV14]. While these changes to the basic Poisson solver here are nominal and left to the reader, increasing the differential order of the energy requires specific attention (see Section 6). Before this, we discuss two important considerations during discretization.

5.2. Quadrature

When discretizing the integral in Equation (21), we must approximate the partial volume of tetrahedra straddling the overlap boundaries. We compared various strategies. We specifically *avoid* computing this analytically or splitting elements as this is tantamount to the mesh boolean problem and would inherit its numerical challenges and robustness issues. Instead, we observe that numerical quadrature or Monte Carlo sampling improves accuracy and indeed help convergence, albeit with diminishing returns (see Figure 10). Approximating this integral is simpler than remeshing. We avoid computing exact intersections or new combinatorics.

Unless otherwise noted, we simply treat an element as fractionally inside or outside another mesh by averaging the number of domains each corner positions lies within (i.e., first-order quadrature).

5.2.1. Constraint Thinning

The simplest way to extend our boundary coupling constraints for $K = 2$ in Equation (18) is to consider all possible pairs of the K subdomains:

$$u_{ai} = \sum_{j=1}^{n_b} u_{bj} \varphi_{bj}(\mathbf{v}_{ai}) \quad \forall i, a \neq b \text{ such that } \mathbf{v}_{ai} \in \partial\Omega_a \cap \Omega_b. \tag{22}$$

For shapes where many subdomains overlap on the same region, a boundary vertex of one subdomain may show up in > 1 other subdomains, resulting in equality constraints for each. This unnecessarily reduces the search space and tarnishes the solution near the overlap boundary (see Figure 11). Much like in [PTSZ11], the transitivity

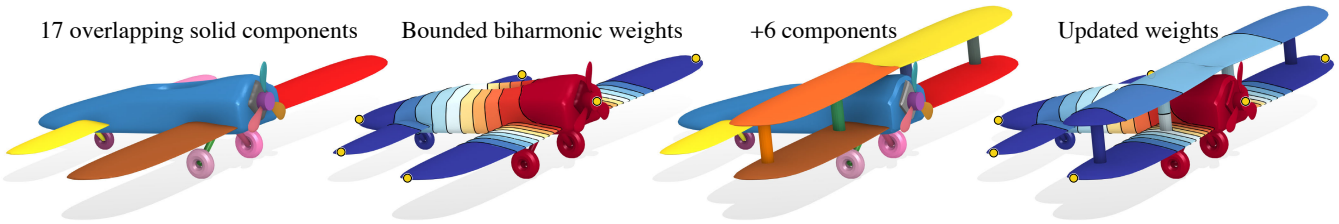

Figure 12: *Updating the shape with another stack of wings does not require updating a unified tet mesh. Instead new components are tet-meshed independently and added to the system algebraically.*

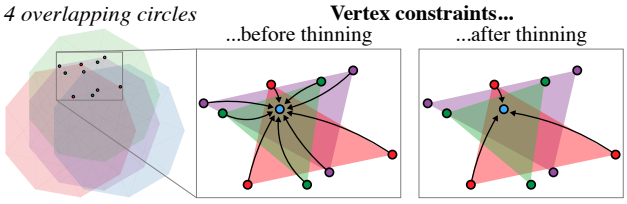

Figure 13: *Pair-wise constraints on multiple overlapping subdomains lead to redundancy, which we remove via constraint thinning. The highlighted vertex of the blue mesh in this didactic example is interpolated by elements in the green, red and purple meshes, when only one of these would be necessary.*

of the equality above makes it so that we only *need* one coupling constraint for each boundary vertex. We cannot be satisfied with finding *any* maximal spanning tree of constraints since that may still concentrate constraints near a single vertex.

We experimented with various heuristics for picking which constraint to keep for each fixed vertex. Removing all but the first constraint creates a slight bias to the arbitrary ordering of the domains. Selecting a random constraint works reasonably well, but still results in many vertices involved in multiple constraints. Averaging or softening constraints also helps, but increases complexity.

Ideally we would like to maximize the total number of vertices involved in the constraints (to diffuse the constraints) while still ensuring exactly one constraint per overlap-boundary vertex. Viewing the constraint matrix $\mathbf{A}$ as graph, this selection is a form of vertex cover problem.

We approximate the maximum cover by *scoring* vertices based on how many constraints they are involved in; similarly, we score each constraint by averaging the scores of the vertices involved. For each vertex involved in more than one constraint, we keep the least saturated (lowest scored) constraint only and remove the rest, as shown in Figure 13. *Thinning* the constraints in this way significantly helps avoid issues near boundaries when multiple shapes overlap (see Figure 11). The decrease in the number of constraints also reduces the linear system size, albeit with marginal affect on performance.

6. Higher-Order Partial Differential Equations

Methods in geometry processing often go beyond second-order PDEs to model problems requiring smoother continuity at constraints [BK04a, SLCO*04, JTSZ10, SGWJ17] or higher-order control [FSH11, JC08] (see Figure 12). Returning briefly to the smooth setting, we focus on the squared Laplacian energy to extend our consideration of deconstructed domains to higher-order PDEs:

$$\min_u \int_\Omega (\Delta u)^2 \, dA, \tag{23}$$

resulting in the fourth-order bi-Harmonic equation:

$$\Delta^2 u(\mathbf{x}) = 0 \qquad \forall \mathbf{x} \in \Omega. \tag{24}$$

The second derivatives of this energy are not immediately discretizable using linear FEM, so we introduce an auxiliary function z and solve the equivalent constrained minimization problem:

$$\min_{u,z} \int_\Omega z^2 \, dA, \tag{25}$$

$$\text{subject to } \Delta u(\mathbf{x}) = z(\mathbf{x}) \qquad \forall \mathbf{x} \in \Omega. \tag{26}$$

Applying the Lagrange multiplier method and Green's identity, this transforms into a saddle problem involving only first derivatives:

$$\operatorname*{saddle}_{u,z,\mu} \int_\Omega \left(z^2 + \nabla\mu \cdot \nabla u + \mu z \right) dA + \text{ boundary terms} \tag{27}$$

where μ is the Lagrange multiplier function and we defer discussion of boundary terms to previous works (e.g., [SGWJ17]).

We now have a problem involving only first derivatives which we can discretize using multiple sets of linear finite elements (i.e., mixed FEM). After factoring out μ, the resulting system has the symmetric matrix form of a KKT system:

$$\begin{pmatrix} \mathbf{0} & \mathbf{L}^\mathsf{T} \\ \mathbf{L} & -\mathbf{M} \end{pmatrix} \begin{pmatrix} \mathbf{u} \\ \mathbf{z} \end{pmatrix} = \begin{pmatrix} \mathbf{0} \\ \mathbf{0} \end{pmatrix} \tag{28}$$

6.1. Unsuccessful Low-Order Boundary-Only Coupling

While the second-order Poisson equation requires one set of boundary conditions (e.g., fixed values or fixed normal derivatives), the fourth-order bi-Laplace equation in Equation (24) requires two sets of boundary conditions to identify a unique solution. For example, we can fix both the value *and* the normal derivative along the boundary $\partial\Omega$ (i.e., fix low-order quantities). If we explicitly fix *only* the value along the boundary when minimizing the squared Laplacian energy, then *natural boundary conditions* will emerge to ensure uniqueness (cf. [SGWJ17]). This also occurs in the mixed FEM discretization. Fixing only the value along the overlapping region for two subdomains $\Omega_1 \cap \Omega_2$ couples the function values together, but

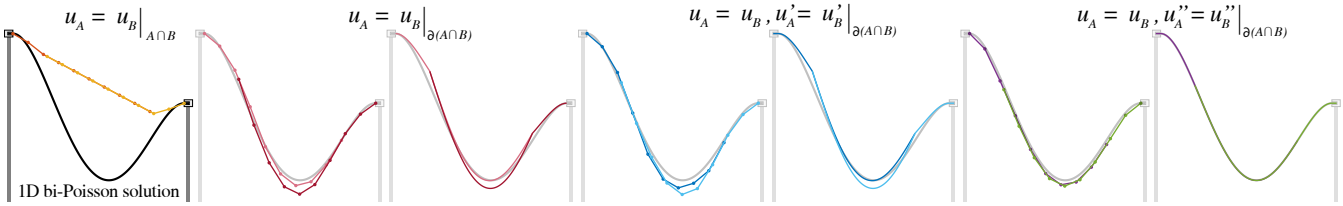

Figure 14: *Enforcing equality at* all vertices *of two overlap domains results in locking (red & yellow). For higher-order PDEs, coupling* by value alone *at overlap boundaries avoids extreme locking, but resolution refinement reveals non-smoothnesses (pinks). Attempting to enforce derivative continuity by coupling values and first derivatives results in* local locking *and non-smoothness persists (blues). We couple primary values* and *auxiliary values constrained to the Laplacian (u'' in 1D) at sub-domain boundaries: the solution is smooth (purple & green).*

produces a noticeable "kink" (see Figure 14). We are witnessing the natural boundary conditions on one subdomain's function (in this case $\Delta u = 0$) disagreeing with the derivatives of *other* subdomain's function: i.e., in general, $\Delta u_1 = 0 \neq \Delta u_2$ on $\partial\Omega_1 \cap \Omega_2$.

To take advantage of the same uniqueness properties used in Section 5, we must ensure that each function is sufficiently constrained with boundary conditions. One idea would be to trivially extend our boundary-only coupling by fixing the value *and* normal derivative along the overlapping boundary:

$$u_1(\mathbf{x}) = u_2(\mathbf{x}) \qquad \forall \mathbf{x} \in \partial(\Omega_1 \cap \Omega_2), \qquad (29)$$

$$\nabla u_1(\mathbf{x}) \cdot \mathbf{n}(\mathbf{x}) = \nabla u_2(\mathbf{x}) \cdot \mathbf{n}(\mathbf{x}) \qquad \forall \mathbf{x} \in \partial(\Omega_1 \cap \Omega_2), \qquad (30)$$

where $\mathbf{n}(\mathbf{x})$ is the normal vector pointing outward from the overlapping region $\Omega_1 \cap \Omega_2$. In the smooth setting, we can quickly confirm that this is equivalent to the original energy minimization problem in Equation (23) following the same reasoning in Section 5.

These *low-order* coupling constraints are simple to discretize using linear FEM, but unfortunately do not lead to a convergent system. Fixing directional derivatives across the two functions leads to harmonic locking locally (the one-ring of vertices at the overlapping region boundary). This region shrinks with mesh refinement, but the problem persists: effectively the solution locks so that natural boundary conditions emerge, albeit one-ring into the overlapping domain (see Figure 14).

6.2. Higher-Order Boundary-Only Coupling

Fortunately, the bi-Laplace equation in Equation (24) is also uniquely determined by other combinations of boundary conditions. Such combinations of low- and high-order conditions sometimes appear directly during problem modeling (e.g., [JC08]). The introduction of the auxiliary variable $z = \Delta u$ in Equation (25), makes the choice of fixing the value and the Laplacian of u along the boundary particularly easy to describe:

$$u_1(\mathbf{x}) = u_2(\mathbf{x}) \qquad \forall \mathbf{x} \in \partial(\Omega_1 \cap \Omega_2), \qquad (31)$$

$$z_1(\mathbf{x}) = z_2(\mathbf{x}) \qquad \forall \mathbf{x} \in \partial(\Omega_1 \cap \Omega_2). \qquad (32)$$

During discretization using mixed FEM, we add these constraints to the Lagrangian's KKT system in Equation (28) directly, resulting in

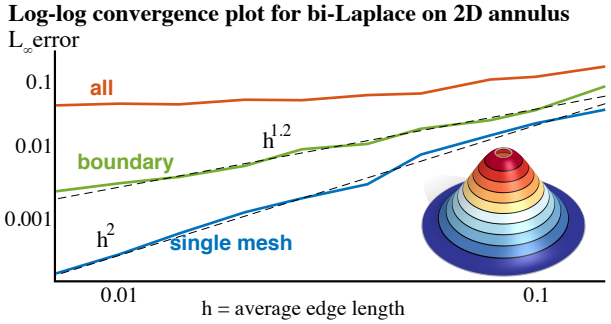

Figure 15: *The behavior of our different sets of constraints for the bi-Laplace equation $\Delta^2 u = 0$ mirrors that of the Poisson equation solver shown previously.*

a larger KKT system:

$$\begin{pmatrix} \mathbf{0} & \mathbf{L}^\mathsf{T} & \mathbf{A}^\mathsf{T} & \mathbf{0} \\ \mathbf{L} & -\mathbf{M} & \mathbf{0} & \mathbf{A}^\mathsf{T} \\ \mathbf{A} & \mathbf{0} & \mathbf{0} & \mathbf{0} \\ \mathbf{0} & \mathbf{A} & \mathbf{0} & \mathbf{0} \end{pmatrix} \begin{pmatrix} \mathbf{u} \\ \mathbf{z} \\ \lambda_u \\ \lambda_z \end{pmatrix} = \begin{pmatrix} \mathbf{0} \\ \mathbf{0} \\ \mathbf{0} \\ \mathbf{0} \end{pmatrix}, \qquad (33)$$

where $\lambda_u, \lambda_z \in \mathbb{R}^{n_1+n_2}$ are vectors of Lagrange multipliers enforcing boundary coupling constraints on $\mathbf{u}$ and $\mathbf{z}$ respectively, and $\mathbf{A}$ is the linear constraint matrix. While the constraints on the values in $\mathbf{u}$ are straightforward, the constraints on the auxiliary values $\mathbf{z}$ may be interpreted as acting orthogonally to the original mixed FEM constraint that $\mathbf{Mz} = \mathbf{L}u$.

This discretization avoids the "kink" of the low-order boundary coupling in Section 6.1 (see Figure 14). We see convergence with respect to mesh refinement (see Figure 15).

A remaining issue with our discretization is that mixed FEM results in a saddle problem, rather than a standard convex, linearly constrained quadratic energy minimization. However, this is overcome by rearranging terms algebraically (see Appendix B).

7. Experiments & Results

We have implemented our method using MATLAB using finite element operators from GPTOOLBOX [J*16] and point location routines from LIBIGL [JP*18]. We use TETGEN [Si03] to mesh the subdomains in all examples except the sphere and 3D annulus test cases,

Shape	#Tets	K	Build **A**	Problem	Solve
Android	113118	33	0.56 s	BBW	9.06 s
Bug	159533	16	0.47 s	MSBK	21.73 s
Jet	226548	14	0.48 s	Eigen	1.91 s
Bi-Plane	321237	23	1.05 s	BBW	37.61 s
Microscope	348099	24	1.09 s	Heat	4.84 s
Pistol	412798	18	1.08 s	Wave	4.70 s
Alien	682399	32	2.57 s	Geodesic	13.45 s

Table 1: *Performance timings: #Tets is the total number of tetrahedra across the K overlapping components. We list the runtime for constructing the constraints matrix (*Build **A***) and then conducting the resulting constrained (example-dependent) optimization (*Solve*).*

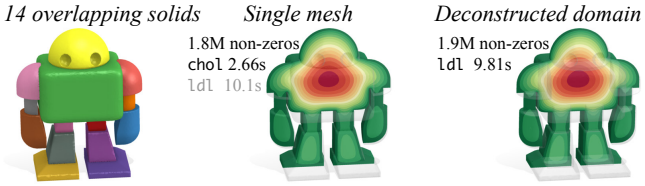

Figure 16: *Traditional mesh-union then tetrahedralization succeeds on this example, enabling an* ad hoc *performance comparison. System matrices for solving the Poisson equation require similar memory, however our* MATLAB *implementation uses LDLT on our resulting Lagrangian: about* 3.7× *slower than Cholesky, here.*

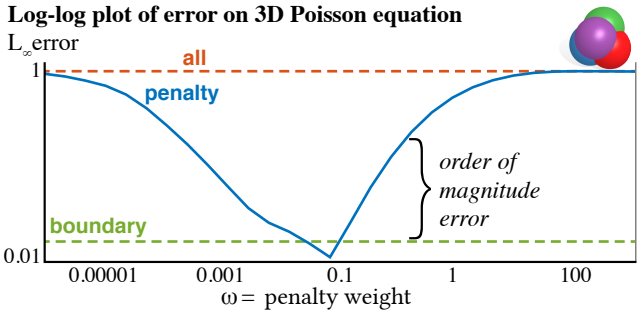

Figure 17: *Weak constraints are sensitive to the penalty weight. There exists a good value (here,* $\omega = 0.1$*), but finding this is non-trivial and problem dependent. An incorrect choice can be disastrous. Our* boundary *coupling is parameterless and achieves low error.*

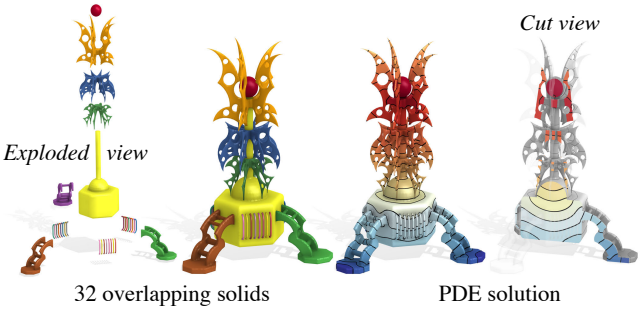

Figure 18: *Following the steps described in [CWW13], we can use our method for computing geodesic distances on a complex shape without a tetrahedral discretization of the domain.*

for which we use QUARTET [DCB13]. We use TRIANGLE [She96] for 2D meshing. On our MacBook Pro with a 3.5GHz Intel Core i7 with 16 GB of memory, the performance bottleneck is always the linear solve (MATLAB's `ldl`), eigen decomposition (MATLAB's `eigs`) or quadratic programming optimization (MOSEK's `quadprog`). For completeness, we list runtime performance in Table 1.

While our main focus is to improve robustness, we observe systematically predictable trends in the runtime performance. For example, consider solving a Poisson equation on a *single mesh* of a solid domain with $O(n^3)$ vertices. For a typical FEM-quality mesh, the performance will be determined by performing a linear system solve on a sparse matrix with $O(n^3)$ non-zeros. In the absence of other constraints, this matrix will be positive definite, affording Cholesky decomposition. For our deconstruction of the same domain into K overlapping components and $O(n^3)$ total vertices across all meshes, we build the *boundary-only* constraints matrix **A** which (under mild assumptions) will contain $O(Kn^2)$ non-zeros. In contrast, fixing *all vertices* in the overlapping region would require $O(Kn^3)$ non-zeros. Using, e.g., the Lagrange multiplier method to enforce our constraints results in an indefinite sparse system matrix with $O(n^3 + Kn^2)$ non-zeros (solved, e.g., with *LDLT*-decomposition). In practice, K is often quite small and the difference in performance between solving on a *single mesh* and a deconstructed domain boils down to the performance of sparse Cholesky versus sparse *LDLT*-decomposition — with the important caveat that solving on a *single mesh* is often impossible without user-intervention. In Figure 16, we found an example where mesh-union followed by tetrahedralization *does* create a useable mesh: Cholesky for the single mesh is roughly 3.7× faster than *LDLT* on our constrained system. As future work, it would be interesting to further exploit our deconstructed domains for performance acceleration and parallelization (see, e.g., [LSLR01]).

An alternative to our boundary-only *hard* constraints would be to enforce *weak* constraints at all vertices in the overlapping regions. In Figure 17, we show that, yes, weak constraints can work, but one must choose the penalty weight carefully. In this experiment, if the penalty is too weak the solutions on different subdomains become decoupled; too strong the solution locks up just as much as the strong constraints. This is not a situation where a different constraint handler will help. For example, the Augmented Lagrangian or Alternating Direction Method of Multipliers (ADMM) methods are numerical techniques for effectively driving the penalty weight to infinity, but in this limit the solution is simply the locked up solution. Meanwhile, the "correct" penalty weight will depend on the mesh resolution, constraint constellation and solution. This may vary spatially: a good weight here may cause locking over there.

We designed 2D and 3D convergence test scenarios (see Figures 7 and 9). We compare L_∞ error to an analytic solution. In Figure 10, we use the same setup to test partial area estimation. For 10-point quadrature, we use the symmetric rules of Zhang et al. [ZCL09].

For irregular tetrahedral meshes, elements overlapping the boundary of another domain typically contain multiple boundary vertices of that domain and thus participate in multiple constraints (even

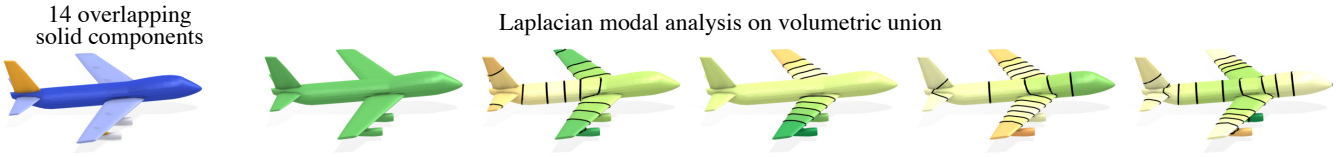

Figure 19: *Our general method can be applied to a variety of problems involving discrete differential geometry including eigen analysis.*

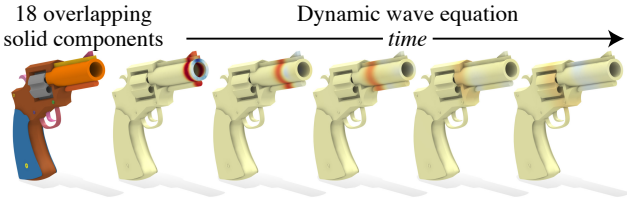

Figure 20: *Our method is accurate enough to repetitive solves for dynamics, such as this shock wave equation simulation.*

in the simple overlapping 3D annuli in Figure 9 *involved* tetrahedra contain on average 3.18 boundary vertices). For more complex shapes, the interior boundaries inherit the irregularity of the overlapping parts. Our method does not smooth or alter these potentially irregular boundaries (see Figure 18).

We demonstrate the versatility of our constraints by expanding beyond the Laplace ($\Delta u = 0$) and Poisson equations ($\Delta u = f$) to other equations found in solid geometry processing. In Figure 1, we demonstrate our boundary only constraints for solving an implicit time step of the heat equation ($u - \delta t \Delta u = u_0$). In Figure 18, we solve the same heat equation for u then the Poisson equation $\Delta\varphi = -\Delta u/|\nabla u|$ to approximate interior distances φ using the method of Crane et al. [CWW13]. In Figure 20, we visualize shock wave through a pistol composed of many overlapping components ($u - \delta t^2 \Delta u = u_0 + \delta t \dot{u}_0$).

In Figure 19, we use our boundary only constraints to conduct a Laplacian modal analysis on a deconstructed domain. We enforce constraints during eigen decomposition via the null space method [Gol73], but replace the QR decomposition with the sparser LUQ decomposition. In Figure 21, we quantitatively validate our method using the Laplacian spectrum. The smallest one hundred eigenvalues using our method match the theoretical groundtruth for a sphere domain (and those computed using standard linear FEM on a single mesh). To extend this comparison to a more complex example where theoretical values are not known, we found a shape where mesh-union followed by tetrahedralization succeeds. Compared to second-order finite differences over a high-resolution voxelization, our spectrum better matches the spectrum found using a single unified mesh. Higher-order elements — known to improve spectral convergence [RBG*09] — could be used in either method, but do not affect our main contribution of setting up constraints.

By rearranging our higher-order coupling for bi-Laplacian problems in Section 6.2 into a convex energy minimization (see Appendix B) we can immediately implement advanced methods involving L_1 sparsity inducing norms for shape descriptors, such as the multiscale pre-biharmonic kernels [Rus11] in Figure 22 and inequality constraints such as the bounded biharmonic weights [JBPS11], used for real-time skinning deformations in Figure 23. In Figure 12,

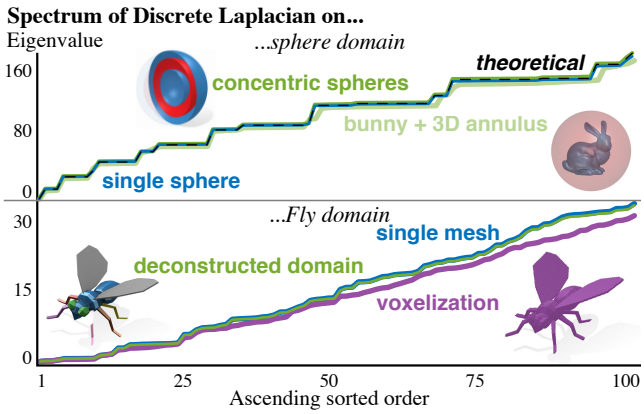

Figure 21: *The spectral behaviour of our Laplacian operator constructed using solely the information from the primitive's meshes (green lines) approaches the analytical spectra (left) in the same way as that obtained from traditional FEM on a unified mesh of the domain (left and right, blue line).*

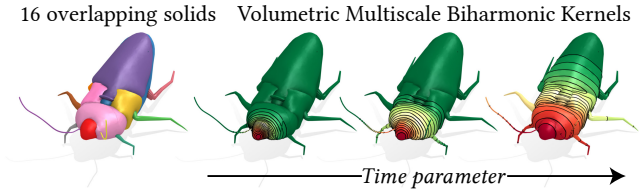

Figure 22: *Our high-order boundary coupling constraints complement advanced biharmonic energy-minimization methods and additional constraints such as L_1 sparsity.*

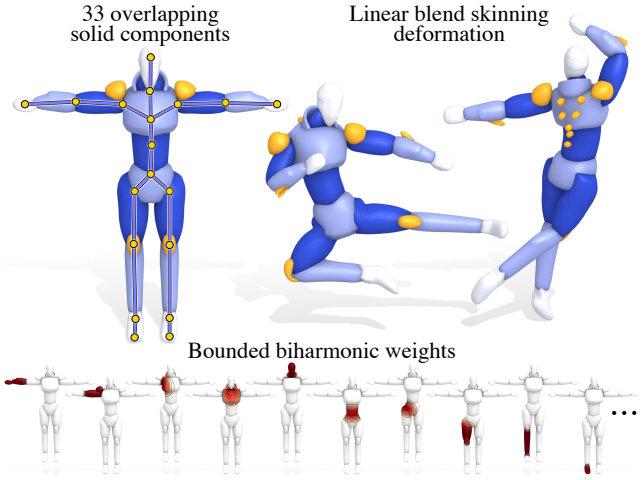

Figure 23: *Minimizing the squared Laplacian subject to bound constraints produces automatic deformation bases: our method enables this over deconstructed domains.*

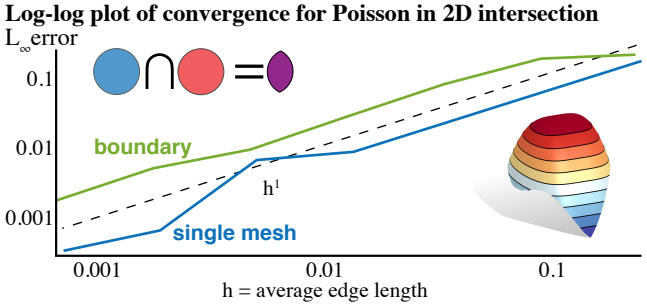

Figure 24: *Our method can be generalized to deal with other two-dimensional set operations, such as intersections and substractions.*

we demonstrate the robustness of our method to large-scale geometry changes. Wings are added to the plane simply by overlapping new solid components: we only need to tet-mesh the new components and add their linear constraints to the system. In the classic geometry processing pipeline, we would need to invoke mesh union and fragile global tet-meshing algorithms. Our method avoids this.

8. Limitations & Future Work

We make a heavy assumption that the input domain is or can be deconstructed into simple tetrahedralizable subdomains. While many models are originally created using constructive solid geometry (CSG) operations, often only the (typically poor triangle-quality) mesh-boolean result is available when it comes time to solve a volumetric PDE. Therefore, we advocate to *retain* these simpler domains and the construction tree rather than preemptively resolving the mesh-boolean. Nonetheless, our tetrahedralizers, TETGEN [Si03] and QUARTET [DCB13], still occasionally fail even on simpler subdomains. To mitigate this we can preprocess problematic subdomains on a case-by-case basis using MESHFIX [Att10] and generalized winding numbers [BDS*18]. In this paper, we consider volumetric unions of polyhedral subdomains. Other domains such as those modeled using metaball implicits [WMW86] or reconstructed from unstructured point clouds (e.g., [KBH06]) are not immediately suitable for our method. It is exciting to consider automatic methods for converting such domains into unions of simpler primitives, perhaps with inspiration from advances in approximate convex decomposition [AGCO13].

While all examples presented in this paper deal exclusively with unions of different shapes, one can conceive of certain variations that would make our method valid for all CSG operations, such as intersections or differences. We have promising initial results for intersecting two-domains in 2D (see Figure 24) and are working an extension to full 3D CSG trees.

References

[AA00] ANDERSEN E. D., ANDERSEN K. D.: The MOSEK interior point optimizer for linear programming: an implementation of the homogeneous algorithm. In *High Performance Optimization*. 2000.

[ACSYD05] ALLIEZ P., COHEN-STEINER D., YVINEC M., DESBRUN M.: Variational tetrahedral meshing. *ACM Trans. Graph.* (2005).

[AGCO13] ASAFI S., GOREN A., COHEN-OR D.: Weak convex decomposition by lines-of-sight. *ACM Trans. Graph.* (2013).

[Att10] ATTENE M.: A lightweight approach to repairing digitized polygon meshes. *Vis. Comput.* (2010).

[BBK05] BOTSCH M., BOMMES D., KOBBELT L.: Efficient linear system solvers for mesh processing. *IMA Mathematics of Surfaces* (2005).

[BDS*18] BARILL G., DICKSON N., SCHMIDT R., LEVIN D. I., JACOBSON A.: Fast winding numbers for soups and clouds. *ACM Trans. Graph.* (2018).

[Ben85] BENEK J.; BUNING P. S. J.: A 3-d chimera grid embedding technique. In *7th Computational Physics Conference* (1985).

[BF09] BERNSTEIN G., FUSSELL D.: Fast, exact, linear booleans. In *Proc. SGP* (2009).

[BGF15] BARKI H., GUENNEBAUD G., FOUFOU S.: Exact, robust, and efficient regularized booleans on general 3d meshes. *Computers and Mathematics with Applications* (2015).

[BK04a] BOTSCH M., KOBBELT L.: An intuitive framework for real-time freeform modeling. *ACM Trans. Graph. 23*, 3 (2004).

[BK04b] BOTSCH M., KOBBELT L.: A remeshing approach to multiresolution modeling. In *Proc. SGP* (2004), pp. 189–196.

[BS15] BERCOVIER M., SOLOVEICHIK I.: Overlapping non-matching meshes domain decomposition method in isogeometric analysis. *arXiv preprint arXiv:1502.03756* (2015).

[BSD83] BENEK J., STEGER J., DOUGHERTY F.: A flexible grid embedding technique with application to the euler equations. In *AIAA Comp. Fluid Dynamics Conf.* (1983).

[BTST12] BHARAJ G., THORMÄHLEN T., SEIDEL H.-P., THEOBALT C.: Automatically rigging multi-component characters. *Comput. Graph. Forum 30*, 2 (2012).

[CDS12] CHENG S.-W., DEY T. K., SHEWCHUK J.: *Delaunay mesh generation*. CRC Press, 2012.

[CFD12] CUILLIÈRE J.-C., FRANÇOIS V., DROUET J.-M.: Automatic 3d mesh generation of multiple domains for topology optimization methods. In *IMR* (2012).

[CK10] CHAUDHURI S., KOLTUN V.: Data-driven suggestions for creativity support in 3d modeling. *ACM Trans. Graph.* (2010).

[CKGK11] CHAUDHURI S., KALOGERAKIS E., GUIBAS L., KOLTUN V.: Probabilistic reasoning for assembly-based 3D modeling. *ACM Trans. Graph.* (2011).

[CWW13] CRANE K., WEISCHEDEL C., WARDETZKY M.: Geodesics in heat: A new approach to computing distance based on heat flow. *ACM Trans. Graph.* (2013).

[Dav06] DAVIS T. A.: CHOLMOD*: a sparse supernodal Cholesky factorization and modification package, version 3.0*. Univ. of Florida, 2006.

[DCB13] DORAN C., CHANG A., BRIDSON R.: Isosurface stuffing improved: Acute lattices and feature matching. *SIGGRAPH Talks* (2013).

[DHB*16] DA F., HAHN D., BATTY C., WOJTAN C., GRINSPUN E.: Surface-only liquids. *ACM Trans. Graph.* (2016).

[DMYN08] DOBASHI Y., MATSUDA Y., YAMAMOTO T., NISHITA T.: A fast simulation method using overlapping grids for interactions between smoke and rigid objects. *Comput. Graph. Forum* (2008).

[DMZ*17] DEVITO Z., MARA M., ZOLLHÖFER M., BERNSTEIN G., RAGAN-KELLEY J., THEOBALT C., HANRAHAN P., FISHER M., NIESSNER M.: Opt: A domain specific language for non-linear least squares optimization in graphics and imaging. *ACM Trans. Graph.* (2017).

[EB15] EDWARDS E., BRIDSON R.: The discretely-discontinuous galerkin coarse grid for domain decomposition. *CoRR* (2015).

[EQYF13] ENGLISH R. E., QIU L., YU Y., FEDKIW R.: Chimera grids for water simulation. In *Proc. SCA* (2013).

[For97] FORTUNE S.: Vertex-rounding a three-dimensional polyhedral subdivision. *Discrete Comput. Geom* (1997).

[FSH11] FINCH M., SNYDER J., HOPPE H.: Freeform vector graphics with controlled thin-plate splines. *ACM Trans. Graph.* (2011).

[GHF86] GOLDFEATHER J., HULTQUIST J. P. M., FUCHS H.: Fast constructive-solid geometry display in the pixel-powers graphics system. In *Proc. SIGGRAPH* (1986).

[GJTP17] GAO X., JAKOB W., TARINI M., PANOZZO D.: Robust hex-dominant mesh generation using field-guided polyhedral agglomeration. *ACM Trans. Graph.* (2017).

[Gol73] GOLUB G. H.: Some modified matrix eigenvalue problems. *SIAM Review* (1973).

[GSLF05] GUENDELMAN E., SELLE A., LOSASSO F., FEDKIW R.: Coupling water and smoke to thin deformable and rigid shells. *ACM Trans. Graph.* (2005).

[GSP*06] GAL R., SORKINE O., POPA T., SHEFFER A., COHEN-OR D.: Non-realistic expressive modeling. In *SIGGRAPH Sketches* (2006).

[HDA17] HERHOLZ P., DAVIS T. A., ALEXA M.: Localized solutions of sparse linear systems for geometry processing. *ACM Trans. Graph.* (2017).

[Hen94] HENSHAW W. D.: A fourth-order accurate method for the incompressible navier-stokes equations on overlapping grids. *JCP* (1994).

[J*16] JACOBSON A., ET AL.: gptoolbox: Geometry processing toolbox, 2016. http://github.com/alecjacobson/gptoolbox.

[JBPS11] JACOBSON A., BARAN I., POPOVIĆ J., SORKINE O.: Bounded biharmonic weights for real-time deformation. *ACM Trans. Graph.* (2011).

[JC08] JOSHI P., CARR N. A.: Repoussé: automatic inflation of 2d artwork. In *Proc. SBIM* (2008), pp. 49–55.

[JMD*07] JOSHI P., MEYER M., DEROSE T., GREEN B., SANOCKI T.: Harmonic coordinates for character articulation. *ACM Trans. Graph.* (2007).

[JP99] JAMES D. L., PAI D. K.: ArtDefo: accurate real time deformable objects. In *Computer Graphics (SIGGRAPH Conference Proceedings)* (New York, NY, USA, 1999), pp. 65–72.

[JP*18] JACOBSON A., PANOZZO D., ET AL.: libigl: A simple C++ geometry processing library, 2018. http://libigl.github.io/libigl/.

[JTSZ10] JACOBSON A., TOSUN E., SORKINE O., ZORIN D.: Mixed finite elements for variational surface modeling. In *Proc. SGP* (2010).

[Kau12] KAUFMANN P.: *Discontinuous Galerkin FEM in Computer Graphics*. PhD thesis, ETH Zurich, 2012.

[Kaz15] KAZHDAN M.: Fast and exact poisson solvers on symmetric geometries. *Comput. Graph. Forum* (2015).

[KBH06] KAZHDAN M., BOLITHO M., HOPPE H.: Poisson surface reconstruction. In *Proc. SGP* (2006).

[KFS13] KRISHNAN D., FATTAL R., SZELISKI R.: Efficient preconditioning of laplacian matrices for computer graphics. *ACM Trans. Graph.* (2013).

[KKRC97] KIRIS C., KWAK D., ROGERS S., CHANG I.-D.: Computational approach for probing the flow through artificial heart devices. *Biomech. Eng.* (1997).

[LS07] LABELLE F., SHEWCHUK J. R.: Isosurface stuffing: fast tetrahedral meshes with good dihedral angles. In *ACM Trans. Graph.* (2007).

[LSLR01] LOEHNER R., SHAROV D., LUO H., RAMAMURTI R.: Overlapping unstructured grids. In *39th Aero. Sciences Meeting & Exhibit* (2001).

[MDSB03] MEYER M., DESBRUN M., SCHRÖDER P., BARR A. H.: Discrete differential-geometry operators for triangulated 2-manifolds. In *Visualization and Mathematics III* (2003).

[MGL*15] MALGAT R., GILLES B., LEVIN D. I. W., NESME M., FAURE F.: Multifarious hierarchies of mechanical models for artist assigned levels-of-detail. In *Proc. SCA* (2015).

[Nak99] NAKAHASHI KAZUHIRO; TOGASHI F. S. D.: An intergrid-boundary definition method for overset unstructured grid approach. In *14th Computational Fluid Dynamics Conference* (1999).

[Pes73] PESKIN C.: Flow patterns around heart valves: a digital computer method for solving the equations of motion. *IEEE Transactions on Biomedical Engineering* (1973).

[PTSZ11] PIETRONI N., TARINI M., SORKINE O., ZORIN D.: Global parametrization of range image sets. *ACM Trans. Graph.* (2011).

[RBG*09] REUTER M., BIASOTTI S., GIORGI D., PATANÈ G., SPAGNUOLO M.: Discrete laplace–beltrami operators for shape analysis and segmentation. *Computers & Graphics* (2009).

[Rus11] RUSTAMOV R. M.: Multiscale biharmonic kernels. In *Proc. SGP* (2011).

[SBGG04] SMITH B., BJORSTAD P., GROPP W., GROPP W.: *Domain Decomposition: Parallel Multilevel Methods for Elliptic Partial Differential Equations*. Cambridge University Press, 2004.

[SBSCO06] SHARF A., BLUMENKRANTS M., SHAMIR A., COHEN-OR D.: SnapPaste: an interactive technique for easy mesh composition. *Vis. Comput. 22*, 9 (2006), 835–844.

[Sch70] SCHWARZ H.: Übereinen grenzübergang durch alternierendes verfahren. *Vierteljahrsschrift der Naturforschenden Gesellschaft in Zürich 15:272-286* (1870).

[SCV14] SOLOMON J., CRANE K., VOUGA E.: Laplace-beltrami: The swiss army knife of geometry. In *SGP Courses* (2014).

[SGWJ17] STEIN O., GRINSPUN E., WARDETZKY M., JACOBSON A.: Natural boundary conditions for smoothing in geometry processing. *CoRR* (2017).

[She96] SHEWCHUK J. R.: Triangle: Engineering a 2D quality mesh generator and delaunay triangulator. In *Applied Comp. Geometry*. 1996.

[She02] SHEWCHUK J. R.: What is a good linear element? interpolation, conditioning, and quality measures. In *Proc. IMR* (2002).

[Si03] SI H.: TETGEN: A 3D delaunay tetrahedral mesh generator, 2003.

[SLCO*04] SORKINE O., LIPMAN Y., COHEN-OR D., ALEXA M., RÖSSL C., SEIDEL H.-P.: Laplacian surface editing. In *Proc. SGP* (2004).

[SPSH*17] SHTENGEL A., PORANNE R., SORKINE-HORNUNG O., KOVALSKY S. Z., LIPMAN Y.: Geometric optimization via composite majorization. *ACM Trans. Graph.* (2017).

[SRUL16] SOKOLOV D., RAY N., UNTEREINER L., LÉVY B.: Hexahedral-dominant meshing. *ACM Trans. Graph.* (2016).

[SS10a] SCHMIDT R., SINGH K.: *Drag, drop, and clone: An interactive interface for surface composition*. Tech. rep., Univ. of Toronto, 2010.

[SS10b] SCHMIDT R., SINGH K.: Meshmixer: an interface for rapid mesh composition. In *ACM SIGGRAPH Talks* (2010).

[SVB17] SOLOMON J., VAXMAN A., BOMMES D.: Boundary element octahedral fields in volumes. *ACM Trans. Graph.* (2017).

[SVJ15] SACHT L., VOUGA E., JACOBSON A.: Nested cages. *ACM Trans. Graph.* (2015).

[WMKG07] WARDETZKY M., MATHUR S., KÄLBERER F., GRINSPUN E.: Discrete Laplace operators: no free lunch. In *Proc. SGP* (2007).

[WMW86] WYVILL G., MCPHEETERS C., WYVILL B.: Soft objects. In *Advanced Computer Graphics* (1986).

[ZCL09] ZHANG L., CUI T., LIU H.: A set of symmetric quadrature rules on triangles and tetrahedra. *Computational Mathematics* (2009).

[ZGZJ16] ZHOU Q., GRINSPUN E., ZORIN D., JACOBSON A.: Mesh arrangements for solid geometry. *ACM Trans. Graph.* (2016).

[ZJ16] ZHOU Q., JACOBSON A.: Thingi10k: A dataset of 10,000 3d-printing models. *CoRR* (2016).

[ZT00] ZIENKIEWICZ O., TAYLOR R.: *The Finite Element Method*. Butterworth-Heinemann, 2000.

Appendix A: Deconstructed Domains Solver

This appendix provides a step-by-step construction of the discrete solver for deconstructed domains.

Without loss of generality let us assume three-dimensional domains ($d = 3$). The input to our method is a set of K overlapping, embedded, manifold tetrahedral meshes with vertices $\{\mathbf{V}_1, \ldots, \mathbf{V}_K\}$ so that $\mathbf{V}_i \in \mathbb{R}^{n_i \times 3}$ contains the positions of the ith subdomain's n_i vertices in its rows and list of tetrahedral indices $\{\mathcal{T}_1, \ldots, \mathcal{T}_K\}$ where the row-indices into $\mathbf{V}_i$ of the ith subdomain's t_i tetrahedra appear as rows $\mathcal{T}_i \in [1, \ldots, n_i]^{t_i \times 4}$.

We first build the constraint matrix $\mathbf{A} \in \mathbb{R}^{(b_1+\ldots+b_K)\times(n_1+\ldots+n_K)}$, where b_i are the number of boundary vertices of the ith mesh lying inside a tetrahedron of *any* other mesh.

Next we build the sparse discrete gradient matrix $\mathbf{G}_i \in \mathbb{R}^{3t_i \times n_i}$ for each domain and compute *adjusted* volumes for each tetrahedron $\mathbf{a}_i \in \mathbb{R}^{t_i}$ (accounting for the $1/\sum_{j=1}^{K} \chi_j$ term in Equation (21), see Section 5.2).

From these we can construct a quadratic coefficients matrix (i.e., discrete Laplacian) $\mathbf{L}_i \in \mathbb{R}^{n_i \times n_i}$ for each domain:

$$\mathbf{L}_i = \mathbf{G}_i^{\mathsf{T}} \operatorname{diag}(\mathbf{a}_i)\, \mathbf{G}_i, \tag{34}$$

where $\operatorname{diag}(\mathbf{x})$ for a vector $\mathbf{x} \in \mathbb{R}^n$ creates $n \times n$ matrix with $\mathbf{x}$ along the diagonal. We concatenate the contributions from each subdomain into a monolithic Laplacian $\mathbf{L} \in \mathbb{R}^{(n_1+\ldots+n_K)\times(n_1+\ldots+n_K)}$,

$$\mathbf{L} = \operatorname{blkdiag}(\mathbf{L}_1, \ldots, \mathbf{L}_K), \tag{35}$$

where $\operatorname{blkdiag}(\mathbf{A}, \mathbf{B}, \ldots)$ creates a block diagonal matrix from matrices $\mathbf{A}$, $\mathbf{B}$, ...

Using the adjusted tetrahedral volumes in $\mathbf{a}_i$, we build a "barycentric" lumped diagonal mass matrix for each mesh $\mathbf{M}_i \in \mathbb{R}^{n_i \times n_i}$ and stack these as well to create the mass matrix of the entire system $\mathbf{M} \in \mathbb{R}^{(n_1+\ldots+n_K)\times(n_1+\ldots+n_K)}$,

$$(\mathbf{M}_i)_{jj} = \sum_{k \in N(j)} \tfrac{1}{4} (\mathbf{a}_i)_k \tag{36}$$

$$\mathbf{M} = \operatorname{blkdiag}(\mathbf{M}_1, \ldots, \mathbf{M}_K), \tag{37}$$

where $N(j)$ are the tetrahedra incident on vertex j. Further accuracy could possibly be achieved by using a hybrid "Voronoi" mass matrix [MDSB03, JTSZ10].

Finally, we define $\mathbf{u} \in \mathbb{R}^{(n_1+\ldots+n_K)}$ as the vertically stacked vectors of unknown per-vertex values across the K subdomain meshes.

We may now pose the discretization of the energy minimization problem in Equations (21-22) using a standard matrix form:

$$\min_{u} \mathbf{u}^{\mathsf{T}} \mathbf{L} \mathbf{u} - \mathbf{u}^{\mathsf{T}} \mathbf{M} \mathbf{1} \tag{38}$$

$$\text{subject to } u_{ij} = g(\mathbf{v}_{ij}) \qquad \forall \mathbf{v}_{ij} \in \partial\Omega \cap \partial\Omega_i \tag{39}$$

$$\text{and } \mathbf{A}\mathbf{u} = \mathbf{0} \tag{40}$$

where $\mathbf{1}$ and $\mathbf{0}$ are vectors ones and zeros respectively. Vertices receiving boundary conditions or constraints are identified combinatorially and located inside other meshes efficiently using a spatial acceleration data structure (e.g., we use LIBIGL's AABB tree [JP*18]), then *thinned* by removing rows according to our approximate max-cover criteria (see Section 5.2.1). We use the MATLAB or MOSEK quadratic programming solvers to find an optimal $\mathbf{u}$.

Appendix B: Rearrangement into Quadratic Minimization

A remaining issue with our discretization is that mixed FEM results in a saddle problem, rather than a standard convex, linearly constrained quadratic energy minimization. This means in practice we cannot send the system in Equation (33) to a standard quadratic programming solvers because the top-left sub-block

$$\begin{pmatrix} \mathbf{0} & \mathbf{L}^{\mathsf{T}} \\ \mathbf{L} & -\mathbf{M} \end{pmatrix} \tag{41}$$

is not positive semi-definite. However, we can resolve this by factoring out $\mathbf{z} = \mathbf{M}^{-1}(\mathbf{L}u + \mathbf{A}^{\mathsf{T}}\lambda_z)$ resulting in the smaller KKT system:

$$\begin{pmatrix} \mathbf{L}^{\mathsf{T}}\mathbf{M}^{-1}\mathbf{L} & \mathbf{L}\mathbf{M}^{-1}\mathbf{A}^{\mathsf{T}} & \mathbf{A}^{\mathsf{T}} \\ \mathbf{A}\mathbf{M}^{-1}\mathbf{L}^{\mathsf{T}} & \mathbf{A}\mathbf{M}^{-1}\mathbf{A}^{\mathsf{T}} & \mathbf{0} \\ \mathbf{A} & \mathbf{0} & \mathbf{0} \end{pmatrix} \begin{pmatrix} \mathbf{u} \\ \lambda_z \\ \lambda_u \end{pmatrix} = \begin{pmatrix} \mathbf{0} \\ \mathbf{0} \\ \mathbf{0} \end{pmatrix}, \tag{42}$$

where the top-left 2×2 sub-block is now positive semi-definite. This system arrives as the Euler-Lagrange equation for the constrained convex quadratic minimization problem:

$$\min_{\mathbf{u}, \lambda_z} \|\mathbf{M}^{-1/2}(\mathbf{L}\mathbf{u} + \mathbf{A}^{\mathsf{T}}\lambda_z)\|^2 \tag{43}$$

$$\text{subject to } \mathbf{A}\mathbf{u} = \mathbf{0}. \tag{44}$$

To avoid inverting the mass matrix and improve the conditioning of the objective term, we introduce another auxiliary variable $\mathbf{y} \in \mathbb{R}^{n_1+n_2}$, arriving at the final constrained problem in standard form:

$$\min_{\mathbf{u}, \lambda_z, \mathbf{y}} \|\mathbf{y}\|^2 \tag{45}$$

$$\text{subject to } \mathbf{A}\mathbf{u} = \mathbf{0}, \tag{46}$$

$$\text{and } \mathbf{L}\mathbf{u} + \mathbf{A}^{\mathsf{T}}\lambda_z = \mathbf{M}^{1/2}\mathbf{y}. \tag{47}$$